INTERNATIONAL JOURNAL FOR NUMERICAL METHODS IN FLUIDS
Int. J. Numer. Meth. Fluids 2002; **38**:1069–1089 (DOI: 10.1002/fld.259)

Analysis of hybrid algorithms for the Navier–Stokes equations with respect to hydrodynamic stability theory

Giuseppe Passoni, Giancarlo Alfonsi*,† and Massimo Galbiati

Dipartimento di Ingegneria Idraulica, Ambientale e del Rilevamento, Politecnico di Milano,
Piazza Leonardo da Vinci 32, 20133 Milano, Italy

SUMMARY

Hybrid three-dimensional algorithms for the numerical integration of the incompressible Navier–Stokes equations are analyzed with respect to hydrodynamic stability in both linear and nonlinear fields. The computational schemes are mixed—spectral and finite differences—and are applied to the case of the channel flow driven by constant pressure gradient; time marching is handled with the fractional step method. Different formulations—fully explicit convective term, partially and fully implicit viscous term combined with uniform, stretched, staggered and non-staggered meshes, x-velocity splitted and non-splitted in average and perturbation component – are analyzed by monitoring the evolution in time of both small and finite amplitude perturbations of the mean flow. The results in the linear field are compared with correspondent solutions of the Orr–Sommerfeld equation; in the nonlinear field, the comparison is made with results obtained by other authors. Copyright © 2002 John Wiley & Sons, Ltd.

KEY WORDS: Navier–Stokes equations; incompressible three-dimensional fluid flow; unsteady channel flow; hybrid spectral-finite difference numerical techniques; linear and nonlinear hydrodynamic stability

1. INTRODUCTION

Among two of the main approaches to the numerical integration of the Navier–Stokes equations —spectral methods and finite difference methods—advantages and disadvantages can be outlined. Spectral methods are highly accurate while difficult to be used in general geometries and grids; they are also mathematically complicated and, as a consequence, not so straightforward to be implemented in computational codes. Finite differences are less complicated methods but they are in general characterized by lower accuracy as compared with spectral algorithms.

With respect to the channel flow problem, purely spectral techniques have been used by Kim *et al.* [1] at $Re = 3300$ (based on channel half width) by using a Fourier–Chebyshev computational algorithm; the time advancement is carried out by means of a semi-implicit

---

*Correspondence to: G. Alfonsi, Dipartimento di Ingegneria Idraulica, Ambientale e del Rilevamento, Politecnico di Milano, Piazza L. da Vinci 32, 20133 Milano, Italy.

†E-mail: giancarlo.alfonsi@polimi.it

Received February 2000
Revised November 2000

scheme as in Moin and Kim [2]: Crank–Nicolson for the viscous term and Adam–Brashforth for the convective term (see also Moin and Kim [3] and Le and Moin [4]). A Fourier–Chebyshev fully spectral method has also been used by Orszag and Kells [5] for the analysis of both linear and nonlinear stability of plane Poiseuille and plane Couette flows, and by Malik *et al.* [6] in which a preconditioned iterative technique has been used to solve the implicit portion of the numerical problem; in Reference [6] the accuracy of the Fourier–Chebychev formulation is compared with that of a mixed Fourier-finite difference algorithm by monitoring the evolution of small amplitude perturbations of the mean flow. Herring *et al.* [7] found (among others) that spectral methods require roughly half as much resolution in space with respect to the finite difference schemes to yield comparable accuracy.

Fully finite difference techniques in conjunction with Sub-Grid Scale models for turbulence simulation have been applied to the case of the plane channel by Deardorff [8], Schumann [9] and Horiuti [10]; in Reference [10] conservative and rotational forms of the Navier–Stokes equations are compared by using a mixed Fourier-finite difference formulation. Rai and Moin [11] developed a spatially high-order-accurate upwind-biased fully finite difference scheme on a staggered grid: they tested their results by monitoring the evolution of small-amplitude disturbances of the mean flow and computing the fully developed channel flow at 3300 for comparison with Reference [1]; they found—among other results—that high-order upwind schemes can yield satisfactory estimates of the evolution of flow instabilities, but a minimum number of grid points is required in order to obtain accurate solutions. Kravcenko and Moin [12] found that aliasing errors are dominant in spectral and high-order finite difference methods, while truncation errors are relevant in low-order finite differences. Tafti [13] performed a study for the comparison of high-order formulations with second-order central-difference schemes for the numerical integration of the Navier–Stokes equations; one of his final conclusions is that high-order finite difference schemes do not add sufficiently greater accuracy to the results, to justify the extra computational effort associated with their use.

Mixed algorithm have also been tested; a spectral-finite differences scheme for the Navier–Stokes equations in the plane channel has been developed by Garg *et al.* [14]. In space, they used Fourier decomposition in the homogeneous directions and finite differences in the direction orthogonal to the solid walls; in time, a semi-implicit scheme was used, third-order Runge–Kutta for the convective terms and the planar horizontal viscous terms, and Crank–Nicolson for the vertical viscous term.

Overall, a certain number of computational codes for the Navier–Stokes equations applied to the channel flow case and based on fully spectral, fully finite difference and hybrid spectral-finite difference algorithms can be found in the literature, but very seldom are they tested with respect to hydrodynamic stability theory; moreover, and exception made for Reference [6], such tests are limited to purely spectral (Reference [5] reports the only test in the nonlinear field) or purely finite difference schemes.

The aim of this work is to assess the properties of a number of hybrid spectral-finite difference numerical algorithms for the Navier–Stokes equations applied to the case of the channel flow, with respect to hydrodynamic stability in both linear and nonlinear fields (see Reference [15] for a detailed description of the basic algorithm). Hydrodynamic stability is a fundamental test for numerical schemes for viscous fluid flow equations and is related to both accuracy and numerical dissipation [16–18].

Hydrodynamic stability in the channel flow can be briefly summarized by distinguishing between linear stability (evolution of small amplitude perturbations of the mean flow) and stability in the nonlinear field (evolution of finite amplitude perturbations) (see also the review of Bayly *et al.* [19]). In the linear field, the evolution of small amplitude perturbations can be monitored by comparing the numerical solutions given by Navier–Stokes algorithms with that of the Orr–Sommerfeld equation; this part is discussed in Section 4 (Section 2 is devoted to the description of the numerical schemes and Section 3 to preliminary tests). Squire's theorem can also be recalled: if, at a given Reynolds number, an unstable three-dimensional disturbance exists, an unstable two-dimensional disturbance exists at a lower value of the Reynolds number. As a consequence, the first unstable mode must be two-dimensional.

There is no theory for the evolution of finite amplitude perturbations. Early work in this field has been performed experimentally: Klebanoff *et al.* [20], Patel and Head [21] and Kao and Park [22] (a comparison with the results of Reference [22] can be found in Tatsumi and Yoshimura [23]) found that the transition Reynolds number depends on both spectrum and amplitude of the two- and three-dimensional induced disturbances. In the numerical field, Herbert [24, 25] analyzed both two- and three-dimensional finite amplitude perturbations with respect to the stability of the channel flow by using a fully spectral Fourier–Chebyshev technique. A study about instability and transition to turbulence in plane Poiseuille and plane Couette flows has been performed by Orszag and Kells [5]; they used a fully spectral numerical algorithm of the same type as Herbert's and considered both two- and three-dimensional finite amplitude disturbances. Section 5 of this work is devoted to the presentation of the nonlinear stability tests that have been performed in this research with the use of hybrid spectral-finite difference discretizations; further discussion and comparisons with Reference [5], are provided.

2. NUMERICAL SCHEMES

The incompressible Navier–Stokes equations in non-dimensional conservative form and the continuity equation are considered (index notation, $i, j = 1, 2, 3$, summation convention applies):

$$\partial_t u_i + \partial_j (u_i u_j) = -\partial_i p + \frac{1}{Re} \partial_j \partial_j u_i \tag{1}$$

$$\partial_i u_i = 0 \tag{2}$$

where Re is the Reynolds number. Spatial coordinates and velocity components are named x, y, z and u, v, w, respectively; variables are non-dimensionalized by using the channel half-width (h) and the steady-state centerline velocity ($u_{\max}$); the flow fields are admitted to be periodic in x and z (the physical streamwise and spanwise directions, see Figure 1 for a plot of the system geometry) and the system of the governing equations is Fourier-transformed in those directions. The nonlinear terms of the momentum equation are evaluated pseudo-spectrally, by anti-transforming the velocities in physical space and performing the products: to avoid aliasing errors the 2/3 rule has been enforced. The spatial derivatives along y are evaluated by means of a second-order centered finite difference scheme (see Reference [15] for further details).

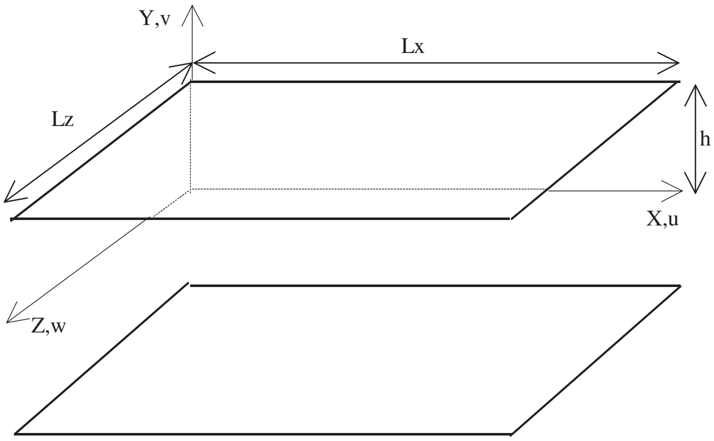

Figure 1. The computational domain.

Scheme 1.

The x-component of the velocity is considered to be the sum of a mean part $\bar{u}=\bar{u}(y,t)$ and a perturbation $u'=u'(x,y,z,t)$; this decomposition can be relevant—with respect to round-off errors—when u^2 quantities with small $u's$ have to be computed. The whole convective term and the x and z viscous terms are incorporated in the following definitions:

$$C_u(\bar{u},\hat{u}',\hat{v}',\hat{w}') = ik_x(2\bar{u}\hat{u}' + \hat{u}'^2) + \frac{\partial(\bar{u}\hat{v}' + \widehat{u'v'})}{\partial y} + ik_z(\bar{u}\hat{w}' + \widehat{u'w'}) + \frac{1}{Re}k^2\hat{u}' \tag{3a}$$

$$C_v(\bar{u},\hat{u}',\hat{v}',\hat{w}') = ik_x(\bar{u}\hat{v}' + \widehat{v'u'}) + \frac{\partial(\hat{v}'^2)}{\partial y} + ik_z(\widehat{v'w'}) + \frac{1}{Re}k^2\hat{v}' \tag{3b}$$

$$C_w(\bar{u},\hat{u}',\hat{v}',\hat{w}') = ik_x(\bar{u}\hat{w}' + \widehat{w'u'}) + \frac{\partial(\widehat{w'v'})}{\partial y} + ik_z(\hat{w}'^2) + \frac{1}{Re}k^2\hat{w}' \tag{3c}$$

where '^' denotes the Fourier-transformed variables and $k^2 = k_x^2 + k_z^2$. The time advancement is performed by means of a semi-implicit technique: a fourth-order Runge–Kutta scheme is used for the terms in Equations (3), while a second-order Crank–Nicolson scheme is used for the viscous term along the direction orthogonal to the solid walls (y); a uniform, staggered mesh is used. For each Fourier mode the following equations hold:

$$\begin{aligned}\hat{u}'(t+\Delta t) = \hat{u}'(t) &- \frac{1}{6}\Delta t(C_{u_0} + 2C_{u_1} + 2C_{u_2} + C_{u_3})\\ &+ \frac{1}{Re}\Delta t\,\frac{1}{2}\left(\frac{\partial^2\hat{u}'(t+\Delta t)}{\partial y^2} + \frac{\partial^2\hat{u}'(t)}{\partial y^2}\right) - ik_x\hat{\phi}\end{aligned} \tag{4a}$$

$$\hat{v}'(t+\Delta t) = \hat{v}'(t) - \frac{1}{6}\Delta t(C_{v_0} + 2C_{v_1} + 2C_{v_2} + C_{v_3}) + \frac{1}{Re}\Delta t\frac{1}{2}\left(\frac{\partial^2\hat{v}'(t+\Delta t)}{\partial y^2} + \frac{\partial^2\hat{v}'(t)}{\partial y^2}\right) - \frac{\partial\hat{\phi}}{\partial y} \tag{4b}$$

$$\hat{w}'(t+\Delta t) = \hat{w}'(t) - \frac{1}{6}\Delta t(C_{w_0} + 2C_{w_1} + 2C_{w_2} + C_{w_3}) + \frac{1}{Re}\Delta t\frac{1}{2}\left(\frac{\partial^2\hat{w}'(t+\Delta t)}{\partial y^2} + \frac{\partial^2\hat{w}'(t)}{\partial y^2}\right) - ik_z\hat{\phi} \tag{4c}$$

The system of equations to be numerically solved (besides continuity) is composed of three equations in the perturbation components of the velocity and one equation in the mean part of the x-velocity:

$$\bar{u}(t+\Delta t) = \bar{u}(t) + \frac{1}{Re}\Delta t\frac{1}{2}\left(\frac{\partial^2\bar{u}(t+\Delta t)}{\partial y^2} + \frac{\partial^2\bar{u}(t)}{\partial y^2}\right) - \Delta t\left(\overline{\frac{\partial p}{\partial x}}\right) \tag{5}$$

In Equations (4), $\hat{\phi}$ is the average of the perturbation pressure over Δt. At each substep of the Runge–Kutta procedure, the fractional step method [26, 27] is applied: intermediate variables are introduced, mass conservation is enforced, the pressure equation is solved and the intermediate values of the velocity are corrected with the pressure. The implicit part of the time advancement procedure and the spatial finite difference discretization in the direction orthogonal to the solid walls bring to linear systems of algebric equations of tridiagonal type: the Thomas algorithm is used for their solution. Boundary conditions of no slip at the walls and periodic conditions in the streamwise and spanwise directions, have been imposed.

Scheme 1a.

To explore the influence of grid stretching near the walls where the steepest gradients are present, two stretching laws for the grid points along y have been introduced; (i) geometric progression:

$$\Delta y_j = G\Delta y_{j-1} \tag{6}$$

where G is a weighting factor ($G = 0.96$ in most simulations), and (ii) hyperbolic tangent:

$$y_{str} = Py + (1-P)\left(1 - \frac{\tanh[Q(1-y)]}{\tanh Q}\right) \tag{7}$$

where P and Q are two parameters characterizing the distribution (P and $Q = 1.9$ in most simulations). The partial derivatives along y are calculated accordingly.

Scheme 1b.

In Scheme 1, a staggered mesh in all directions is used. The staggered mesh enhances the conservation properties of the numerical discretizations but also introduces numerical dissipation where interpolations are performed, particularly within the process of pseudo-spectral evaluation of the nonlinear terms. Scheme 1b utilizes a mesh staggered only along y (hereinafter named nonstaggered); the pressure is collocated at the center of each cell and all three components of the velocity at the same point at the center of the side of the cell orthogonal to y. This choice simplifies the calculation of the nonlinear terms and the implementation of the boundary conditions.

Scheme 2.

In Scheme 1 the viscous term is treated implicitly along y and explicitly along x and z. More stringent accuracy requirements for better representation of turbulent small scales suggest to treat implicitly the whole diffusive part of the equations. In Scheme 2 the convective term is treated explicitly and separated from the viscous term, which is handled implicitly in full, by means of the finite difference scheme. This kind of formulation—numerically rather stable—has been already used in cases of Direct Numerical Simulation of turbulence (*DNS*, see Reference [28] among others). Equations (3) become:

$$C_u(\bar{u},\hat{u}',\hat{v}',\hat{w}') = ik_x(2\bar{u}\hat{u}' + \hat{u}'^2) + \frac{\partial(\bar{u}\hat{v}' + \widehat{u'v'})}{\partial y} + ik_z(\bar{u}\hat{w}' + \widehat{u'w'}) \tag{8a}$$

$$C_v(\bar{u},\hat{u}',\hat{v}',\hat{w}') = ik_x(\bar{u}\hat{v}' + \widehat{v'u'}) + \frac{\partial(\hat{v}'^2)}{\partial y} + ik_z(\widehat{v'w'}) \tag{8b}$$

$$C_w(\bar{u},\hat{u}',\hat{v}',\hat{w}') = ik_x(\bar{u}\hat{w}' + \widehat{w'u'}) + \frac{\partial(\widehat{w'v'})}{\partial y} + ik_z(\hat{w}'^2) \tag{8c}$$

and Equations (4):

$$\begin{aligned}\hat{u}'(t+\Delta t) = \hat{u}'(t) - \frac{1}{6}\Delta t(C_{u_0} + 2C_{u_1} + 2C_{u_2} + C_{u_3}) + \frac{1}{Re}\Delta t\,\frac{1}{2}\bigg(\frac{\partial^2\hat{u}'(t+\Delta t)}{\partial y^2} \\ + \frac{\partial^2\hat{u}'(t)}{\partial y^2} - k^2\hat{u}'(t+\Delta t) - k^2\hat{u}'(t)\bigg) - ik_x\hat{\phi}\end{aligned} \tag{9a}$$

$$\begin{aligned}\hat{v}'(t+\Delta t) = \hat{v}'(t) - \frac{1}{6}\Delta t(C_{v_0} + 2C_{v_1} + 2C_{v_2} + C_{v_3}) + \frac{1}{Re}\Delta t\,\frac{1}{2}\bigg(\frac{\partial^2\hat{v}'(t+\Delta t)}{\partial y^2} \\ + \frac{\partial^2\hat{v}'(t)}{\partial y^2} - k^2\hat{v}'(t+\Delta t) - k^2\hat{v}'(t)\bigg) - \frac{\partial\hat{\phi}}{\partial y}\end{aligned} \tag{9b}$$

$$\begin{aligned}\hat{w}'(t+\Delta t) = \hat{w}'(t) - \frac{1}{6}\Delta t(C_{w_0} + 2C_{w_1} + 2C_{w_2} + C_{w_3}) + \frac{1}{Re}\Delta t\,\frac{1}{2}\bigg(\frac{\partial^2\hat{w}'(t+\Delta t)}{\partial y^2} \\ + \frac{\partial^2\hat{w}'(t)}{\partial y^2} - k^2\hat{w}'(t+\Delta t) - k^2\hat{w}'(t)\bigg) - ik_x\hat{\phi}\end{aligned} \tag{9c}$$

Scheme 3.

By adding up the expressions related to the mean part of the x-velocity $\bar{u}$ and its perturbation component u', one obtains a new formulation, in which in the time marching only three equations are involved; Equations (8) become:

$$C_u(\bar{u},\hat{u}',\hat{v}',\hat{w}') = ik_x(\hat{u}^2) + \frac{\partial(\widehat{uv'})}{\partial y} + ik_z(\widehat{uw'}) \tag{10a}$$

$$C_v(\bar{u},\hat{u}',\hat{v}',\hat{w}') = ik_x(\widehat{v'u}) + \frac{\partial(\hat{v}'^2)}{\partial y} + ik_z(\widehat{v'w'}) \tag{10b}$$

$$C_w(\bar{u},\hat{u}',\hat{v}',\hat{w}') = ik_x(\widehat{w'u}) + \frac{\partial(\widehat{w'v'})}{\partial y} + ik_z(\hat{w}'^2) \tag{10c}$$

and Equations (9):

$$\begin{aligned}\hat{u}'(t+\Delta t) = \hat{u}'(t) &- \frac{1}{6}\Delta t(C_{u_0} + 2C_{u_1} + 2C_{u_2} + C_{u_3})\\ &+ \frac{1}{Re}\Delta t\,\frac{1}{2}\left(\frac{\partial^2\hat{u}'(t+\Delta t)}{\partial y^2} + \frac{\partial^2\hat{u}'(t)}{\partial y^2} - k^2\hat{u}'(t+\Delta t) - k^2\hat{u}'(t)\right) - ik_x\hat{\phi}\\ &+ \Delta t\left(\overline{\frac{\partial p}{\partial x}}\right)\delta_{kx,0}\delta_{kz,0}\end{aligned} \tag{11a}$$

$$\begin{aligned}\hat{v}'(t+\Delta t) = \hat{v}'(t) &- \frac{1}{6}\Delta t(C_{v_0} + 2C_{v_1} + 2C_{v_2} + C_{v_3}) + \frac{1}{Re}\Delta t\,\frac{1}{2}\left(\frac{\partial^2\hat{v}'(t+\Delta t)}{\partial y^2}\right.\\ &\left.+ \frac{\partial^2\hat{v}'(t)}{\partial y^2} - k^2\hat{v}'(t+\Delta t) - k^2\hat{v}'(t)\right) - \frac{\partial\hat{\phi}}{\partial y}\end{aligned} \tag{11b}$$

$$\begin{aligned}\hat{w}'(t+\Delta t) = \hat{w}'(t) &- \frac{1}{6}\Delta t(C_{w_0} + 2C_{w_1} + 2C_{w_2} + C_{w_3}) + \frac{1}{Re}\Delta t\,\frac{1}{2}\left(\frac{\partial^2\hat{w}'(t+\Delta t)}{\partial y^2}\right.\\ &\left.+ \frac{\partial^2\hat{w}'(t)}{\partial y^2} - k^2\hat{w}'(t+\Delta t) - k^2\hat{w}'(t)\right) - ik_z\hat{\phi}\end{aligned} \tag{11c}$$

where δ is the Kroneker delta.

Scheme 4.

A third-order Runge–Kutta algorithm for the time advancement is implemented in the computational codes; the procedure of the fractional step method remains unchanged with respect to Schemes 1–3. In index notation, one has:

$$\begin{aligned}\frac{\hat{u}_i^k - \hat{u}_i^{k-1}}{\Delta t} &= \alpha_k L(\hat{u}_i^{k-2}) + \beta_k L(\hat{u}_i^{k-1}) - \gamma_k N(\hat{u}_i^{k-1})\\ &\quad - \varsigma_k N(\hat{u}_i^{k-2}) - (\alpha_k + \beta_k)\frac{\partial\hat{p}^k}{\partial x_i}\end{aligned} \tag{12}$$

where:

$$L(u_i) = \frac{1}{Re}\partial_j\partial_j u_i \tag{13a}$$

$$N(u_i) = \partial_j(u_i u_j) \tag{13b}$$

Table I. Distinctive characters of the numerical schemes tested.

Scheme	Grid	Convective term	Viscous term	x-velocity
1	staggered uniform	fully explicit 4th-order Runge–Kutta	partially implicit	$u=\bar{u}+u'$
1a	staggered non-uniform	fully explicit 4th-order Runge–Kutta	partially implicit	$u=\bar{u}+u'$
1b	non-staggered non-uniform	fully explicit 4th-order Runge–Kutta	partially implicit	$u=\bar{u}+u'$
2	non-staggered non-uniform	fully explicit 4th-order Runge–Kutta	fully implicit	$u=\bar{u}+u'$
3	non-staggered non-uniform	fully explicit 4th-order Runge–Kutta	fully implicit	u
4	non-staggered non-uniform	fully explicit 3rd-order Runge–Kutta	fully explicit	u

are the diffusive and the convective terms respectively, and $k=1,2,3$ denotes the Runge–Kutta sub-steps. Both advective and viscous terms are treated explicitly (see Reference [4] for the implicit version of this scheme) and:

$$\gamma_1=\frac{8}{15};\quad \gamma_2=\frac{5}{12};\quad \gamma_3=\frac{3}{4}\qquad \varsigma_1=0;\quad \varsigma_2=-\frac{17}{60};\quad \varsigma_3=-\frac{5}{12} \tag{14a}$$

$$\alpha_1=\beta_1=\frac{4}{15};\quad \alpha_2=\beta_2=\frac{1}{15};\quad \alpha_3=\beta_3=\frac{1}{6} \tag{14b}$$

In Table I the distinctive characters of the different formulations are summarized.

3. PRELIMINARY TESTS

Euler test

A first test, particularly directed to the verification of the performance in the calculation of the nonlinear terms with the Runge–Kutta algorithms, has been performed on the Euler equation:

$$\partial_t u_i + \partial_j(u_i u_j) = -\partial_i p \tag{15}$$

Scheme 3 with geometric progression stretching law, has been mainly used. The following—divergence free—initial conditions have been introduced (see also Moin and Kim [3]):

$$u=\varepsilon\frac{L_x}{2}\sin(\pi y)\cos\left(\frac{4\pi x}{L_x}\right)\sin\left(\frac{2\pi z}{L_z}\right)+1 \tag{16a}$$

$$v=-\varepsilon(1+\cos(\pi y))\sin\left(\frac{4\pi x}{L_x}\right)\sin\left(\frac{2\pi z}{L_z}\right) \tag{16b}$$

$$w=-\varepsilon\frac{L_z}{2}\sin\left(\frac{4\pi x}{L_x}\right)\sin(\pi y)\cos\left(\frac{2\pi z}{L_z}\right)+1 \tag{16c}$$

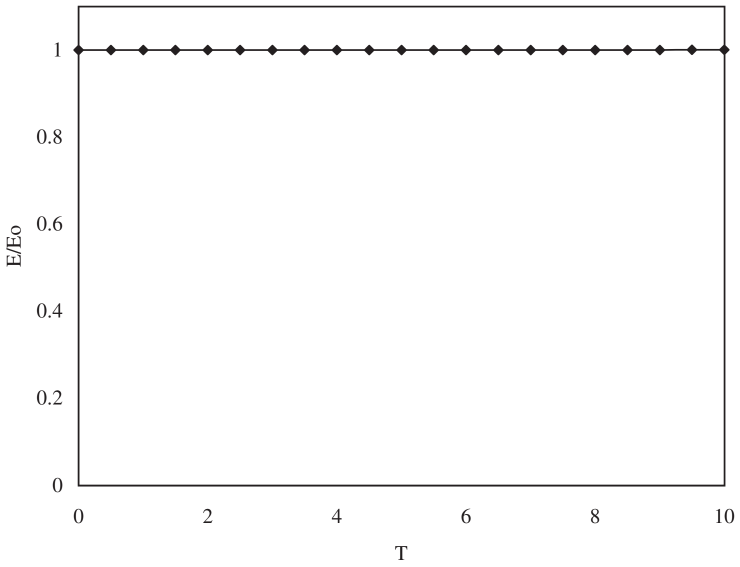

Figure 2. Euler test: evolution of the energy with time (number of x-, y-, z-grid points $N_x = 32$, $N_y = 33$, $N_z = 32$).

where L_x, L_z are the lengths of the computing domain in x and z, respectively and ε is the amplitude ($\varepsilon = 0.01$). In Figure 2 the values of the energy (normalized with respect to the initial value) with time, are reported ($\Delta t = 0.01$).

Burgers test

A second test, particularly directed to the control of the advection–diffusion balance, has been performed by using the one-dimensional (nondimensional) Burgers equation ($0 \leqslant x \leqslant 2\pi$, $0 \leqslant t \leqslant \infty$):

$$\partial_t u + \partial_x (uu) = \frac{1}{Re} \partial_x \partial_x u \tag{17}$$

with:

$$u(x,0) = -\sin(x) \tag{18}$$

as initial condition and $Re = 30$ (see also Huser [29]). The solution is:

$$u(x,t) = -\frac{2}{Re\theta} \frac{\partial \theta}{\partial x} \tag{19}$$

$$\theta(x,0) = \mathrm{e}^{[-\frac{1}{2} Re \cos(x)]} \tag{20}$$

$$\frac{\partial \theta}{\partial t} = \frac{1}{Re} \frac{\partial^2 \theta}{\partial x^2} \tag{21}$$

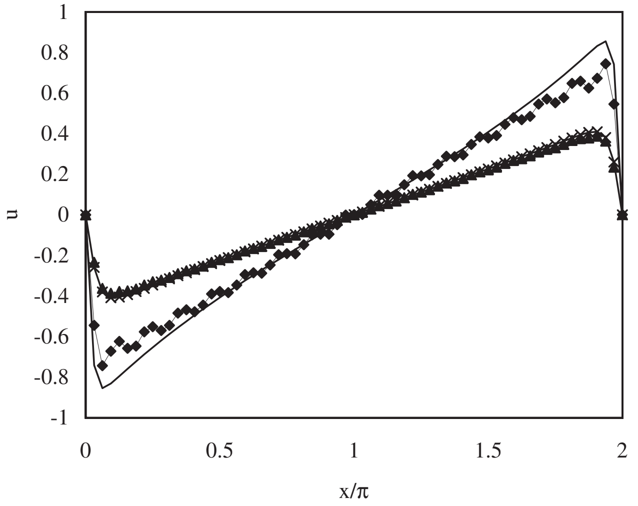

Figure 3. Burgers test: comparison of the numerical solution ((♦) $t=3$, (▲) $t=6$) with the analytical ((–) $t=3$, (×) $t=6$).

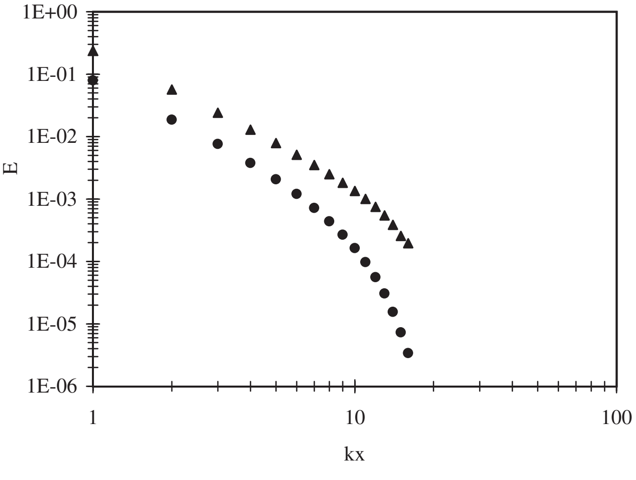

Figure 4. Burgers test: spectra of the numerical solutions ((▲) $t=3$, (•) $t=6$).

Scheme 3 has been mainly used. In Figure 3 the numerical solution of the Burgers equation is compared with the analytical at different nondimensional times. The small discrepancies between numerical results and analytical solution at $t=3$ are due to the influence—at the beginning of the temporal evolution of the calculations—of the initial conditions on the results; already at $t=6$ these differences are no more evident. In Figure 4 the spectra of the numerical solutions are reported ($\Delta t=0.01$).

4. EVOLUTION OF SMALL AMPLITUDE PERTURBATIONS

When small amplitude velocity perturbations, eigensolutions of the Orr–Sommerfeld equation, are superimposed to the steady-state mean velocity profile and integrated in time, the solution arising from the numerical approximation of the Navier–Stokes equations can be compared with that given by the linear fourth-order Orr–Sommerfeld equation (see Reference [30] among others):

$$(U-c)\left[\frac{\mathrm{d}^2\varphi}{\mathrm{d}y^2}-\alpha^2\varphi\right]-\varphi\,\frac{\mathrm{d}^2U}{\mathrm{d}y^2}=\frac{1}{i\alpha Re}\left[\frac{\mathrm{d}^2}{\mathrm{d}y^2}-\alpha^2\right]^2\varphi \tag{22}$$

Equation (22) results from the insertion in the two-dimensional, nearly-parallel, steady-state fluid flow equations ('capital' quantities), of forms of the velocity and the pressure in which three-dimensional perturbations ('primed' quantities) are added to the steady state solutions; in the limit of small amplitudes for the perturbations themselves (linear stability), the terms of order two can be neglected and, as a result of further manipulations, a linear equation in the perturbation field can be obtained. The form of the solution is:

$$u'(x,y,t)=\varepsilon\mathrm{Real}\left[\frac{\mathrm{d}\varphi(y)}{\mathrm{d}y}\,\mathrm{e}^{i\alpha(x-ct)}\right] \tag{23a}$$

$$v'(x,y,t)=\varepsilon\mathrm{Real}[i\alpha\varphi(y)\mathrm{e}^{i\alpha(x-ct)}] \tag{23b}$$

where $\varphi(y)$ is the normalized eigenfunction, ω is the eigenfrequency ($\omega=\omega_r+\omega_i$), α the perturbation wavenumber, $c=(\omega/\alpha),(c=c_r+c_i)$ and ε the perturbation amplitude. The energy associated to the perturbation is:

$$E(t)=\frac{1}{2}\int_{-1}^{1}\int_{0}^{L_x}[u'^2(x,y,t)+v'^2(x,y,t)]\,\mathrm{d}x\,\mathrm{d}y \tag{24}$$

where $L_x=[(2\pi)/(\alpha)]$ (it has been verified that no energy contributions exist in the spanwise direction z, i.e. $w'^2=0$). The linear theory predicts $[E(t))/E_0)]=\mathrm{e}^{2\omega_i t}$, where E_0 is the energy at $t=0$ and ω_i the imaginary part of ω.

The computational tests have been performed at $Re=7500$, with $\alpha=1$, $\varepsilon=0.0001$ (normalized) and the most unstable mode has been considered, characterized by $c=0.24989154+i0.00223498$ ($\Delta t=0.001$). The calculations have been executed up to a nondimensional time $T=50=2t_0$, where t_0 $[t_0=((2\pi)/(\omega_r))=((L_x)/(c_r))]$ represents the time required to cover the distance L_x; different discretizations N_y have been used in the y direction, with a constant 32×4 x, z discretization. In the present calculations the linear theory predictions have been obtained by using a computational code for the numerical solution of the Orr–Sommerfeld equation, based on Orszag's method [31].

In Figure 5 the results of the linear stability tests obtained with the use of Scheme 1 (uniform grid) with different y-discretizations, are reported and compared with the theoretical solution. Figure 6 reports, for comparison, results of the same calculations obtained by Malik *et al.* [6], with the use of their mixed spectral-finite difference algorithm for the numerical solution of the Navier–Stokes equations; among other comments, with 257 grid points along y the results of the present work perform better with respect to the theoretical solution, as compared with Reference [6].

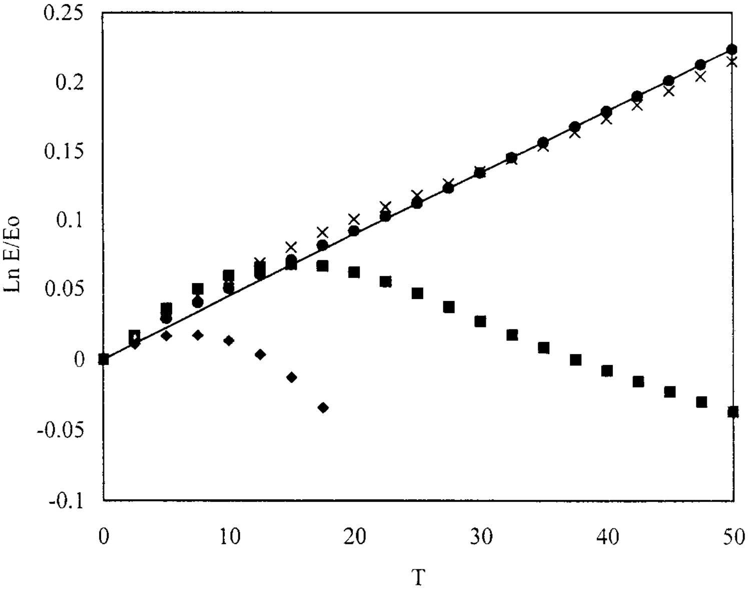

Figure 5. Scheme 1: evolution with time of the energy associated with the small amplitude perturbations ((◆) $N_y = 33$, (■) $N_y = 65$, (×) $N_y = 129$, (•) $N_y = 257$, (–) theory).

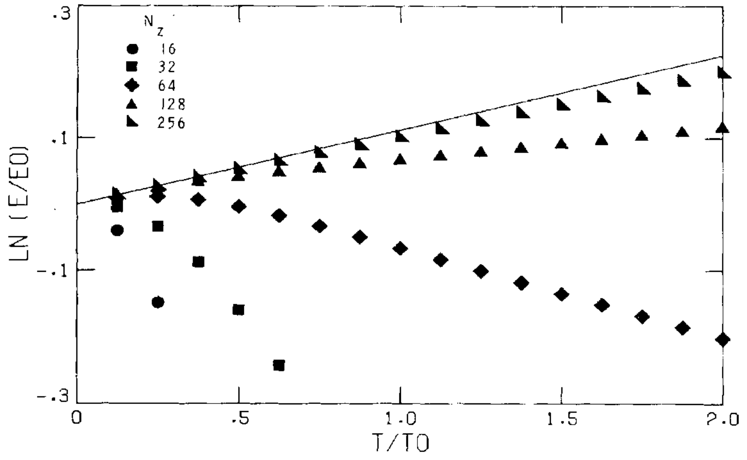

Figure 6. Results of the same linear stability test reported in Figure 5, obtained with a mixed spectral finite difference algorithm by Malik *et al.* [6] with different y-discretizations.

Further calculations have been performed: with two fixed values of the number of grid points in the y direction ($N_y = 65$ and $N_y = 129$), all the different numerical schemes have been tested with respect to linear stability. In Figure 7 (Scheme 1a) results about the influence in the calculations of the use of the two grid streching laws along y (geometric progression and hyperbolic tangent), are reported, together—for better comparison—with the correspondent results obtained with the uniform grid; with the use of a grid stretching law along y, the results

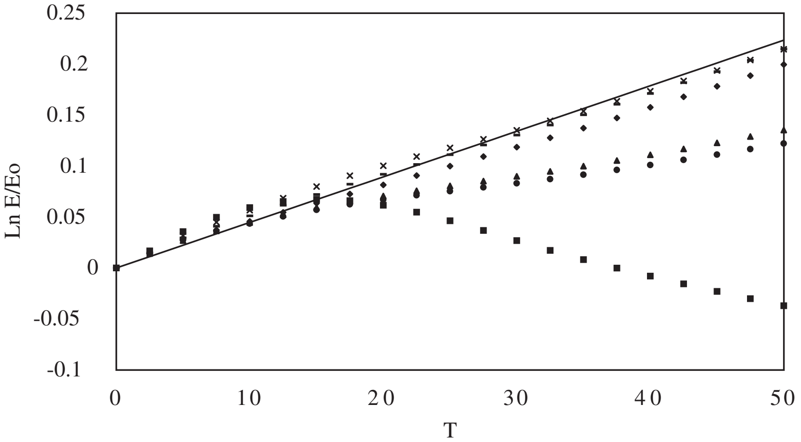

Figure 7. Scheme 1a: evolution with time of the energy associated with the small amplitude perturbations and different grid stretching laws along y ($N_y = 65$, (■) uniform grid, (▲) geometric progression, (●) hyperbolic tangent; $N_y = 129$, (×) uniform grid, (-) geometric progression, (◆) hyperbolic tangent, (–) theory).

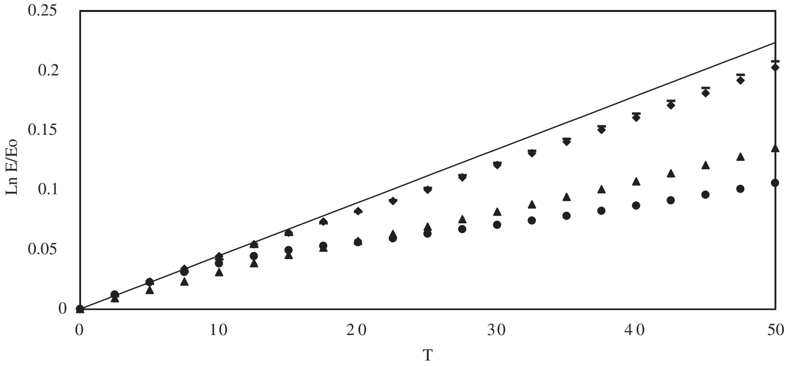

Figure 8. Scheme 1b: evolution with time of the energy associated with the small amplitude perturbations and different grid stretching laws along y ($N_y = 65$, (▲) geometric progression, (●) hyperbolic tangent; $N_y = 129$, (-) geometric progression, (◆) hyperbolic tangent, (–) theory).

are remarkably better with respect to the uniform grid and, of the two stretching laws that have been tested, the geometric progression performs even better with respect to the hyperbolic tangent (in agreement with Rai and Moin [11]). In Figure 8 (Scheme 1b) combined results of the influence of the use of a non-staggered grid together with the use of the two grid stretching laws, are reported. In comparing the results of Figure 8 with Figure 5, the use of a non-staggered grid is more effective at lower values of N_y (and lower nondimensional times), with respect to higher values; also in this case, the geometric progression performs better that the hyperbolic tangent stretching law. In Figure 9, results obtained by running Scheme 2 with the two different grid stretching laws, are reported. No remarkable differences appear with respect to the use of Scheme 1b (Figure 8), meaning that the fully implicit treatment of the viscous

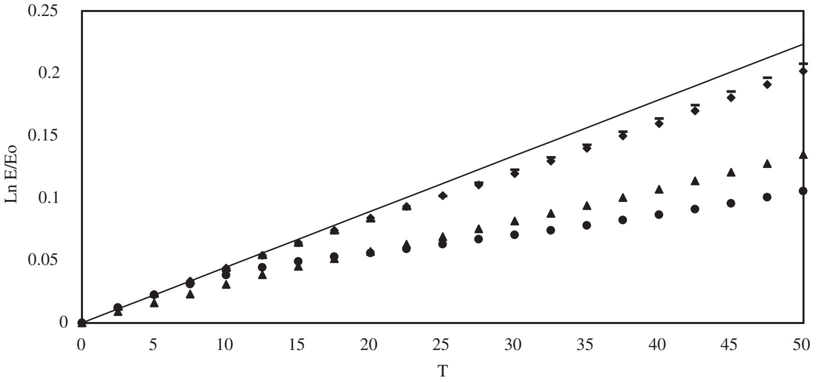

Figure 9. Scheme 2: evolution with time of the energy associated with the small amplitude perturbations and different grid stretching laws along y ($N_y = 65$, (▲) geometric progression, (●) hyperbolic tangent; $N_y = 129$, (-) geometric progression, (◆) hyperbolic tangent, (–) theory).

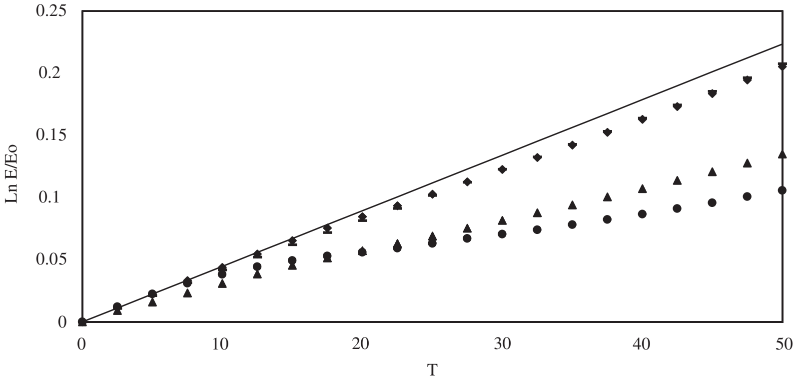

Figure 10. Scheme 3: evolution with time of the energy associated with the small amplitude perturbations and different grid stretching laws along y ($N_y = 65$, (▲) geometric progression, (●) hyperbolic tangent; $N_y = 129$, (-) geometric progression, (◆) hyperbolic tangent, (–) theory).

term performs analogously with respect to its partially implicit treatment (Section 2); the geometric progression performs better than the hyperbolic tangent stretching law. In Figure 10, results obtained by running Scheme 3 with two different grid stretching laws, are reported; the whole computational code is simpler in this case with respect to Scheme 2, and the computations proceed more rapidly; the difference in the results produced by using the two grid streching laws is less pronounced with $N_y = 129$. Figure 11 reports the results obtained with Scheme 4; the use of the 3rd-order Runge–Kutta scheme does not change substantially the level of the accuracy of the results with respect to the use of the 4th-order, according to the stability test in the linear field (evolution of small amplitude perturbations).

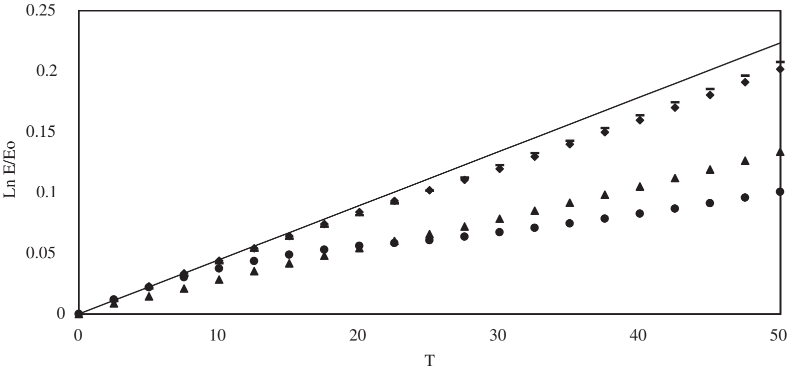

Figure 11. Scheme 4: evolution with time of the energy associated with the small amplitude perturbations and different grid stretching laws along y ($N_y = 65$, (▲) geometric progression, (•) hyperbolic tangent; $N_y = 129$, (-) geometric progression, (◆) hyperbolic tangent, (–) theory).

5. EVOLUTION OF FINITE AMPLITUDE PERTURBATIONS

In summary, instability in the channel flow can be caused by: (i) a two-dimensional small amplitude perturbation (linear field) at values of the Reynolds number greater than 5772 (see Reference [31] among others); (ii) a two-dimensional finite amplitude perturbation (nonlinear field) at values of the Reynolds number greater than 2935 (see References [24, 25]); (iii) a three-dimensional finite amplitude perturbation at values of the Reynolds number close to 1000. In the linear field, the hydrodynamic stability theory enables the calculation of the minimum value of the Reynolds number such as eigenvalues c exist, with $c_i = 0$ (the condition of neutral stability, $Re_{cr} = 5772$, $\alpha_{cr} = 1.02055$, see Orszag [31]).

No theory exists in the nonlinear field, in which stability, besides Re and α, depends also on the perturbation amplitude: critical conditions have to be studied from the analysis of numerical solutions of the Navier–Stokes equations (see for example Herbert [24] in which $Re_{cr} = 2935$ and $\alpha_{cr} = 1.3231$ have been determined for two-dimensional disturbances). Orzag and Kells [5] studied the stability of the channel flow with finite amplitude disturbances as a function of Re, α and the initial value of the perturbation amplitude; they used a fully spectral computational code for the Navier–Stokes equations and obtained accurate results that can be used as a reference case.

To test the properties of the Navier–Stokes discretizations considered in this work with respect to hydrodynamic stability in the nonlinear field, some of the calculations reported in Reference [5] have been executed; finite amplitude perturbations, amplified solutions of the Orr–Sommerfeld equation, have been superimposed to the steady-state mean velocity in the channel. Three tests have been performed: test A, characterized by a perturbation amplitude (ε) decaying with time, test B, with perturbation amplitude stable with time and test C, with perturbation amplitude slightly growing with time, according to Reference [5], respectively (see Table II). Equation (22) has been solved and the most unstable mode has been considered, characterized by $c = 0.328986 + i0.013751$. The form of the perturbation is given by Equation (23) and $\omega = \alpha c = 0.435282 - i0.0181933$.

Table II. Finite amplitude perturbations: characteristic parameters used in the calculations.

	Test A	Test B	Test C
Reynolds number	2935	2935	2935
Perturbation wavenumber (α)	1.3231	1.3231	1.3231
Real ω	0.435282	0.435282	0.435282
Im ω	0.0181933	0.0181933	0.0181933
Initial amplitude (ε)	0.072	0.108	0.182
$N_x \times N_y \times N_z$	$32 \times 129 \times 4$	$32 \times 129 \times 4$	$32 \times 129 \times 4$
Time step Δt	0.001	0.001	0.001
Final time T	100	100	150
Behavior according to Reference [5]	Decay	Neutral	Weak growth

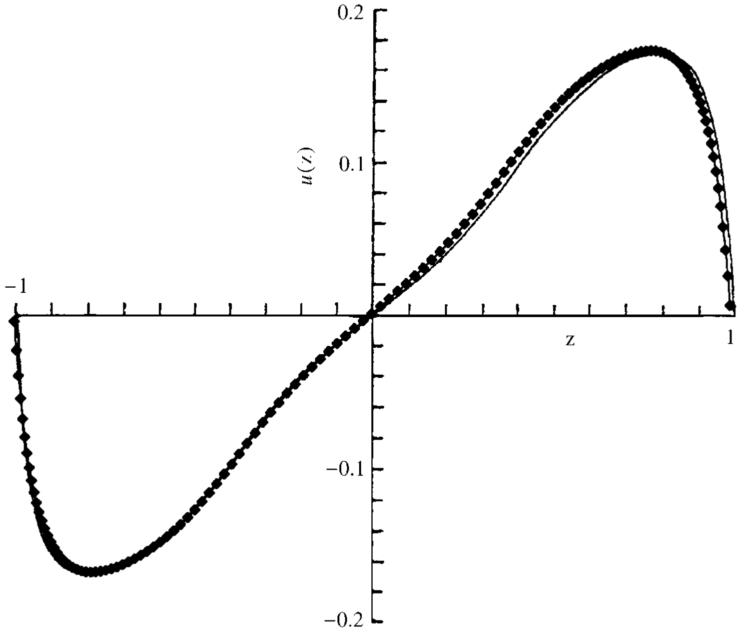

Figure 12. Finite amplitude perturbations. Plot of the y profile of the x-velocity component of the disturbance of test A at $t = 120$ ((♦) present work, (–) Reference [5]).

The results are reported in terms of:

$$A1(t) = \max_y [\hat{u}'(k_x = 1, y, k_z = 0, t)] = A \tag{25a}$$

$$A2(t) = \max_y [\hat{u}'(k_x = 2, y, k_z = 0, t)] = A \tag{25b}$$

where $A1(t)$ is the max in y of the first harmonic and $A2(t)$ is the max in y of the second harmonic (A refers to Figures 15, 16 and 17).

In Figure 12, the plot of the y profile of the x-velocity component of the disturbance of test C is shown at the (nondimensional) time $t = 120$, together with the one reported in Reference [5]. In Figure 13, the plot of the mean velocity $\bar{u}(y)$ of test C at $t = 120$ is shown together

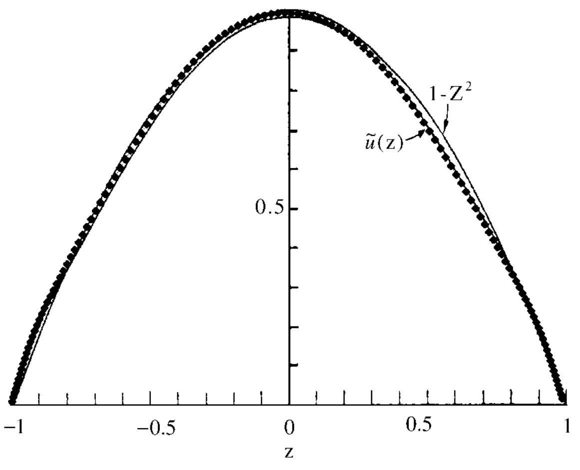

Figure 13. Finite amplitude perturbations. Plot of the mean velocity $\bar{u}(y)$ of test A at $t = 120$ ((◆) present work, (–) correspondent Poiseuille profile, (–) Reference[5]).

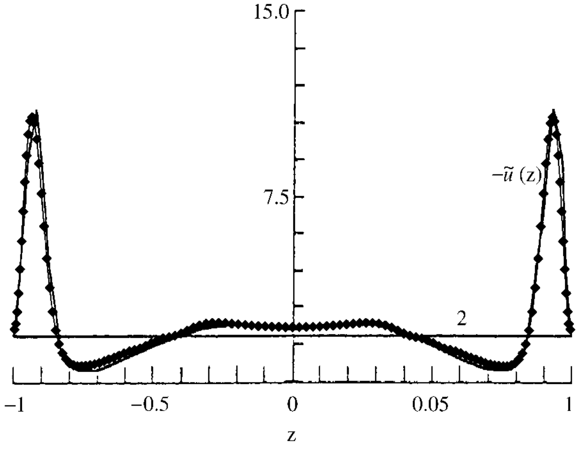

Figure 14. Finite amplitude perturbations. Plot of the curvature $-\bar{u}''(y)$ of the mean velocity profile of test A at $t = 120$ ((◆) present work, (–) curvature of the correspondent Poiseuille profile, (–) Reference [5]).

with the corresponding Poiseuille profile and the one reported in Reference [5]. In Figure 14, the plot of the curvature $-\bar{u}''(y)$ of the mean velocity profile of test C at $t = 120$ is shown together with the curvature of the corresponding Poiseuille profile and the one reported in Reference [5].

The three tests in the nonlinear field have been first executed by using scheme 4; Figures 15, 16 and 17 show the results of tests A, B and C, respectively, obtained with scheme 4; for better comparison, these results have been superimposed to the results of the reference case (Orszag and Kells [5]), showing a satisfactory agreement in all three cases, decay of the perturbation amplitude in case A (Figure 15), stable perturbation in case B (Figure 16) and weak growth in case C.

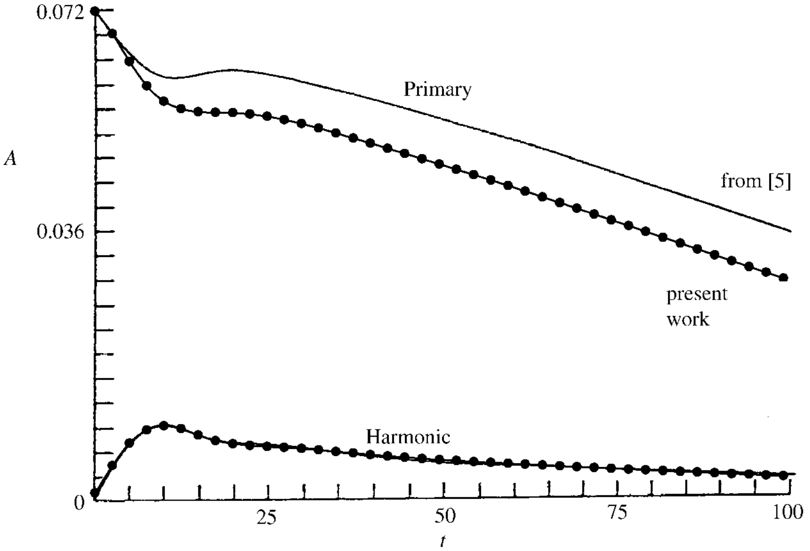

Figure 15. Finite amplitude perturbations, scheme 4, test A. Evolution with time of the maximum amplitude in y, primary (first harmonic) and harmonic (second harmonic, see Reference [5]); (●) present work, (–) results of Reference [5].

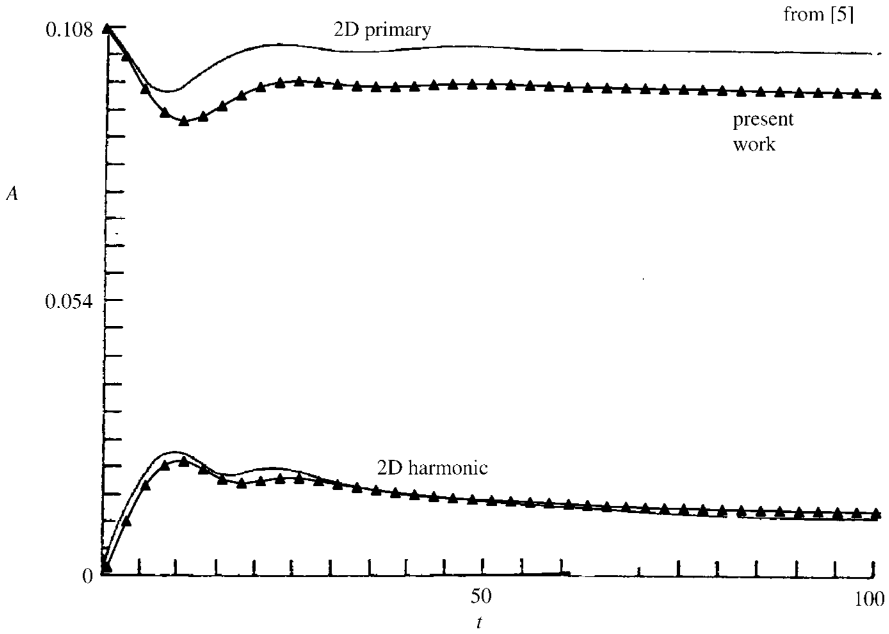

Figure 16. Finite amplitude perturbations, scheme 4, test B. Evolution with time of the maximum amplitude in y, primary (first harmonic) and harmonic (second harmonic, see Reference [5]); (▲) present work, (–) results of Reference [5].

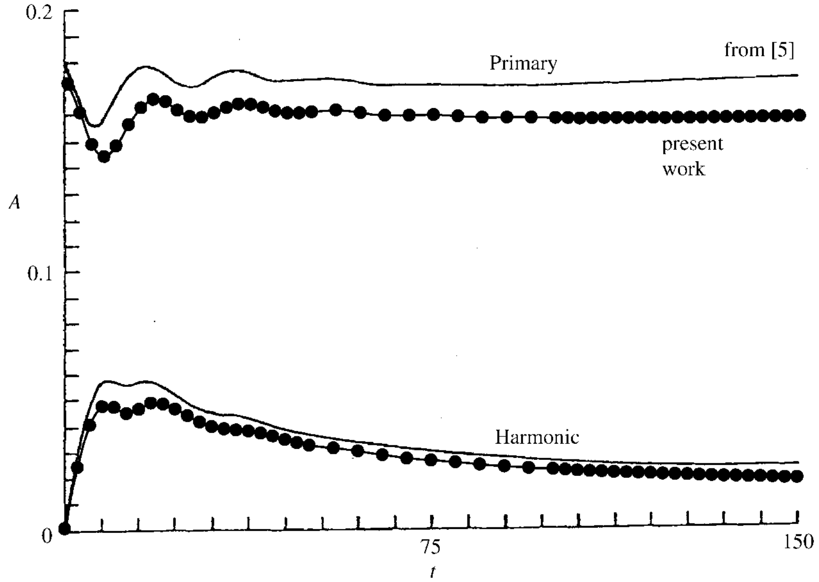

Figure 17. Finite amplitude perturbations, scheme 4, test A. Evolution with time of the maximum amplitude in y, primary (first harmonic) and harmonic (second harmonic, see Reference [5]); (•) present work, (–) results of Reference [5].

Tests A, B and C have also been executed by using scheme 1; the behavior of this scheme has resulted remarkably dissipative in all three cases, especially for what the primary harmonic is concerned; with respect to the dissipative character of scheme 1, the main difference between scheme 1 and scheme 4 consists of the partially implicit vs fully explicit treatment of the viscous term, respectively (see Table I).

6. CONCLUDING REMARKS

Overall, the linear stability tests have shown a satisfactory agreement of the numerical formulations tested in the present work with the theoretical solution offered by the hydrodynamic stability theory. In more detail, the following can be pointed out: (i) the use of a grid stretching law along y produces better results particularly with a limited number of y grid points; (ii) the geometric progression performs generally better than the hyperbolic tangent law, in agreement with Reference [11]; (iii) the use of a grid staggered in one direction only, does not appreciably alter the conservation properties with respect to a grid staggered in all three directions (in both cases $\partial_i v_i \cong 10^{-8}$); (iv) in using scheme 2, no remarkable differences have been noticed between the fully implicit and the partially implicit treatment of the viscous term (Section 2); (v) in using schemes 3 and 4, no remarkable round-off errors have been detected for what the numerical treatment of u is concerned; (vi) no remarkable differences have been detected in using the 3rd-order Runge–Kutta algorithm with respect to the 4th-order.

The calculations performed with finite amplitude perturbations have shown differences in the behaviour of scheme 1 with respect to scheme 4. The results of scheme 4 are in good agreement with Reference [5] (Figures 15, 16, and 17), while those of scheme 1 have shown an excess of dissipation; this circumstance can be explained with the different numerical handling of the viscous term in the two schemes. Thus the stability tests in the nonlinear field have shown differences in the computational schemes, not detectable by limiting the tests to the linear field.

REFERENCES

1. Kim J, Moin P, Moser R. Turbulence statistics in fully developed channel flow at low Reynolds number. *Journal of Fluid Mechanics* 1987; **177**:133–166.
2. Moin P, Kim J. Numerical investigation of turbulent channel flow. *Journal of Fluid Mechanics* 1982; **118**:341–377.
3. Moin P, Kim J. On the numerical solution of time-dependent viscous incompressible fluid flows involving solid boundaries. *Journal of Computational Physics* 1980; **35**:381–392.
4. Le H, Moin P. An improvement of fractional step method for the incompressible Navier–Stokes equations. *Journal of Computational Physics* 1991; **92**:369–379.
5. Orszag SA, Kells LC. Transition to turbulence in plane Poiseuille and plane Couette flow. *Journal of Fluid Mechanics* 1980; **96**:159–205.
6. Malik MR, Zang TA, Hussaini MY. A spectral collocation method for the Navier–Stokes equations. *Journal of Computational Physics* 1985; **61**:64–88.
7. Herring JR, Orszag SA, Kraichnan RH, Fox DG. Decay of two-dimensional homogeneous turbulence. *Journal of Fluid Mechanics* 1974; **66**:417–444.
8. Deardorff JW. A numerical study of three-dimensional turbulent channel flow at large Reynolds numbers. *Journal of Fluid Mechanics* 1970; **41**:453–480.
9. Schumann U. Subgrid scale model for finite difference simulations of turbulent flows in plane channels and annuli. *Journal of Computational Physics* 1975; **18**:376–404.
10. Horiuti K. Comparison of conservative and rotational forms in large eddy simulation of turbulent channel flow. *Journal of Computational Physics* 1987; **71**:343–370.
11. Rai MM, Moin P. Direct simulations of turbulent flow using finite-difference schemes. *Journal of Computational Physics* 1991; **96**:15–53.
12. Kravchenko A, Moin P. On the effect of aliasing and truncation errors in numerical simulations of turbulent flows. *Bulletin of the American Physical Society* 1995; **40**:1944.
13. Tafti D. Comparison of some upwind-biased high-order formulations with a second order central-difference scheme for time integration of the incompressible Navier–Stokes equations. *Computers and Fluids* 1996; **25**:647–665.
14. Garg RP, Ferziger JH, Monismith SG. Hybrid spectral finite difference simulations of stratified turbulent flows on distributed memory architectures. *International Journal for Numerical Methods in Fluids* 1997; **24**:1129–1158.
15. Alfonsi G, Passoni G, Pancaldo L, Zampaglione D. A spectral-finite difference solution of the Navier–Stokes equations in three dimensions. *International Journal for Numerical Methods in Fluids* 1998; **28**:129–142.
16. Chandrasekhar S. *Hydrodynamic and Hydromagnetic Stability*. Oxford University Press: Oxford, 1961.
17. Betchov R, Criminale WO. *Stability of Parallel Flows*. Academic Press: New York, 1967.
18. Drazin PGWM. *Hydrodynamic Stability*. Cambridge University Press: Cambridge, 1981.
19. Bayly BJ, Orszag SA, Herbert T. Instability mechanisms in shear flow transition. *Annual Review of Fluid Mechanics* 1998; **20**:359–391.
20. Klebanoff PS, Tidstrom KD, Sargent LM. The three-dimensional nature of boundary-layer instability. *Journal of Fluid Mechanics* 1962; **12**:1–34.
21. Patel VC, Head MR. Some observations on skin friction and velocity profiles in fully developed pipe and channel flows. *Journal of Fluid Mechanics* 1969; **38**:181–201.
22. Kao TW, Park C. Experimental investigations of the stability of channel flows. Part 1. Flow of a single liquid in a rectangular channel. *Journal of Fluid Mechanics* 1970; **43**:145–164.
23. Tatsumi T, Yoshimura T. Stability of the laminar flow in a rectangular duct. *Journal of Fluid Mechanics* 1990; **212**:437–449.
24. Herbert T. Finite amplitude stability of plane parallel flows. *Laminar-Turbulent Transition*. AGARD-CP 1977; **224**.
25. Herbert T. Secondary instability of plane channel flow to subharmonic three-dimensional disturbances. *Physics of Fluids* 1983; **26**:871–874.
26. Chorin AJ. Numerical solution of the Navier–Stokes equations. *Mathematics and Computations* 1968; **22**:745–762.

27. Kim J, Moin P. Application of a fractional-step method to incompressible Navier–Stokes equations. *Journal of Computational Physics* 1985; **9**:308–323.
28. Moin P, Mahesh K. Direct numerical simulation: a tool in turbulence research. *Annual Review of Fluid Mechanics* 1998; **30**:539–578.
29. Huser A. Direct Numerical Simulation of Turbulent Flow in a Square Duct. Ph.D. Dissertation, Colorado University, 1992.
30. Canuto C, Hussaini MY, Quarteroni A, Zang TA. *Spectral Methods in Fluid Dynamics*. Springer, Verlag: New York, 1987.
31. Orszag SA. Accurate solution of the Orr-Sommerfeld stability equation. *Journal of Fluid Mechanics* 1971; **50**:689–703.